OPTICS

Quantum-enhanced second harmonic generation beyond the photon pairs regime

Thomas Dickinson[1,2]†, Ivi Afxenti[3]†, Giedre Astrauskaite[4], Lennart Hirsch[3], Samuel Nerenberg[4], Ottavia Jedrkiewicz[2,5], Daniele Faccio[4], Caroline Müllenbroich[4], Alessandra Gatti[5], Matteo Clerici[2,3], Lucia Caspani[1,2]*

Two-photon processes are crucial in applications like microscopy and microfabrication, but their low cross section requires intense illumination and limits, e.g., the penetration depth in nonlinear microscopy. Entangled states have been proposed to enhance the efficiency of two-photon interactions and have shown effectiveness at low intensities. This quantum enhancement is generally believed to be lost at high intensities, for more than one photon per mode, raising doubts about its usefulness. We explored experimentally and theoretically two-photon processes driven by entangled photons at intensities beyond this threshold and compared the results with the classical case. We found that a quantum advantage can still be observed at nearly one order of magnitude higher intensities than previously assumed. Our findings show a potential path for exploiting quantum-enhanced two-photon processes in practical applications.

INTRODUCTION

Two-photon interactions underpin several key applications, such as nonlinear imaging (*1*), deep tissue microscopy (*2*), spectroscopy, photodynamic therapy (*3*), data storage, and microfabrication (*4*). In life science applications, such as deep tissue and functional imaging aimed at studying conditions like Alzheimer's disease and other nervous system disorders, increasing the penetration depth of the two-photon process is crucial for sampling in vivo morphology and physiology deeper within tissues without causing damage (*2*). However, the low probability of two photons occupying the same interaction volume necessitates intense laser pulses, which can bleach fluorophores or damage the sample (*5*).

Entangled photon pairs have been suggested as a potential resource to overcome these limitations. They are a defining feature of squeezed vacuum (SV) states routinely produced by parametric down conversion (PDC) in quadratic nonlinear media. Entangled photon pairs can enhance the probability of two-photon processes such as two-photon absorption (TPA) and second harmonic generation (SHG), transforming the interaction into a linear process with a large cross section (*6*–*14*). Entangled TPA (eTPA) is expected to improve the sensitivity of imaging (*8*) and spectroscopy (*15*–*17*), where a reduction of the pump intensity can enable data acquisition with faint, less damaging illumination. It could also allow for the extraction of otherwise inaccessible information, e.g., on collective molecular resonances (*18*, *19*). Despite these promising predictions followed by experimental investigations (*20*–*23*), the advantages brought by eTPA have been debated in recent literature (*24*–*27*). Alternative (classical) mechanisms have been proposed to explain some of the observations (*28*, *29*). Most of the debate focused on the effective value of quantum enhancement and the lack of reproducibility of the experimental results (*25*, *26*, *30*, *31*). These difficulties partially arise from the complexity of molecular fluorophores used in TPA experiments. Large fluorophores feature strong dependencies on temperature and concentration, along with complex excitation pathways and loss mechanisms, which are hard to control and model.

Up to now, the benefits of using squeezed states to enhance two-photon processes have been demonstrated with spatially single-mode radiation at low intensities, where the interaction volume contains less than a photon pair per event (*11*, *32*). In this regime, the quantum advantage stems from the photon pairs behaving as a single particle, which results in a linear relation between the illumination power and the SHG/TPA signal. However, this necessitates low illumination powers and, in turn, results in low nonlinear signals that are of little practical use.

Here, we use sum-frequency processes to investigate two-photon interactions driven by broadband, largely multimode (spatially and temporally) squeezed radiation with a large range of photons per interaction volume. We demonstrate that quantum enhancement persists at illumination levels larger than previously thought (*33*), i.e., at more than one photon per interaction volume. We quantify the quantum enhancement by direct comparison with the classical state typically used for TPA and SHG measurements. With few exceptions (*26*), this is in contrast with most previous studies that compared the case of pure quantum illumination with that of quantum states spoiled by losses (*11*, *32*) or conditioned by postselection to mimic classical radiation (*34*).

We focus on SHG, a simple and easily controllable process that, unlike TPA, does not involve intermediate states of excitation. Furthermore, SHG is a coherent process that can discriminate whether a two-photon signal is generated by entangled or nonentangled photons. This allows us to isolate the quantum enhanced signal [entangled SHG (eSHG), a purely quantum process] from other contributions.

We first investigated the SHG process driven by multimode SV with a low average number of photons per mode (less than one), generated by low-gain PDC. By measuring the eSHG signal, we observed its expected linear scaling with the driving field intensity (*11*), which enabled us to establish the eSHG efficiency and analyze its dependence on optical losses applied to the SV. We then investigated the

[1]Institute of Photonics, Department of Physics, University of Strathclyde, Glasgow G1 1RD, UK. [2]Como Lake Institute of Photonics, Dipartimento di Scienza e Alta Tecnologia, Università degli Studi dell'Insubria, Via Valleggio, 11, 22100 Como, Italy. [3]James Watt School of Engineering, University of Glasgow, Glasgow G12 8QQ, UK. [4]School of Physics and Astronomy, University of Glasgow, Glasgow G12 8QQ, UK. [5]Istituto di Fotonica e Nanotecnologie del CNR, Piazza Leonardo da Vinci 32, 20133 Milano, Italy.
*Corresponding author. Email: lucia.caspani@uninsubria.it
†These authors contributed equally to this work.

SHG driven by SV with many photons per mode, generated by high-gain PDC. It has been assumed that the deterministic recombination of entangled photons, which underpins the linear scaling mentioned above, would quickly become negligible in this regime (*11*, *33*). We demonstrated that this is not the case. We further compared the efficiency of the SHG process driven by multimode SV to that of a classical coherent pulse (standard laser) with the same intensity (same energy, beam size, and pulse duration). We showed that SV drives the SHG process with higher efficiency than a coherent pulse, even when its modes are populated by more than one photon. This direct comparison sheds light on the levels of quantum enhancement that can be expected in real-case scenarios.

Our experimental findings are supported by a theoretical analysis that includes the full spatial and temporal properties of the PDC and the SHG process, predicting that the quantum enhancement is preserved for SV having more than one photon per mode (*35*). Considering our experimental parameters for the optical fields and the nonlinear crystals, the model achieves excellent agreement with the experiments, offering reliable guidance for future investigations.

RESULTS

We have designed our experiment to investigate eSHG driven by pulsed, multimode SV with a controllable number of photons per mode (from below one to far above). The choice of a pulsed source differs from previous works (*11*, *32*) and is required for the generation of SV with a high number of photons per mode (*26*, *34*). A scheme of the setup is shown in Fig. 1A. A 515-nm pump generates a broadband SV via PDC in a 2-mm beta barium borate (BBO) crystal, which is reimaged on a second, identical crystal by an achromatic and dispersion-free telescopic system based solely on reflective optics (see the "Generation of the quantum field" section in Materials and Methods). The spatiotemporal entanglement volume, describing the region where an entangled photon pair is confined, is determined by the overall temporal and angular bandwidths (governed by phase matching and/or spectral filters) and is roughly the inverse of the corresponding spectral volume. A pass-band filter (Brightline FF01-1055/70-25, Semrock) selects the temporal bandwidth of the SV [≃125 THz full width at half maximum (FWHM) corresponding to ≃70 nm around the central wavelength of 1030 nm; see Fig. 1B] to a region where the detrimental impact of the group delay dispersion (GDD) in the nonlinear media, optical elements and coatings is minimal. The angular bandwidth is limited by phase matching to ≃150 mm^{-1} [half width at half maximum (HWHM) corresponding to ≃25 mrad, measured within a 10-nm bandwidth around 1030 nm], as shown in Fig. 1C. This results in an entanglement volume with a ≃11-μm transverse spatial dimension (HWHM, ρ_{ent}) and ≃45-fs duration (FWHM, τ_{ent}), defined from the probability of finding one photon at a distance ρ and delay τ from its twin (see the "Entanglement volume" section in Materials and Methods). The second crystal up-converts the SV, and the generated signal around 515 nm is measured by a photomultiplier tube (PMT). The SHG process can also be driven by the combination of nonentangled photons (*36*–*38*), generating an incoherent second harmonic signal. In contrast, the eSHG process involving entangled photons results in a coherent signal with similar spatiotemporal coherence properties as the PDC pump (*39*). To select only this coherent signal, we filtered the SHG angular and temporal spectrum (see the "Detection of the eSHG" section in Materials and Methods for details).

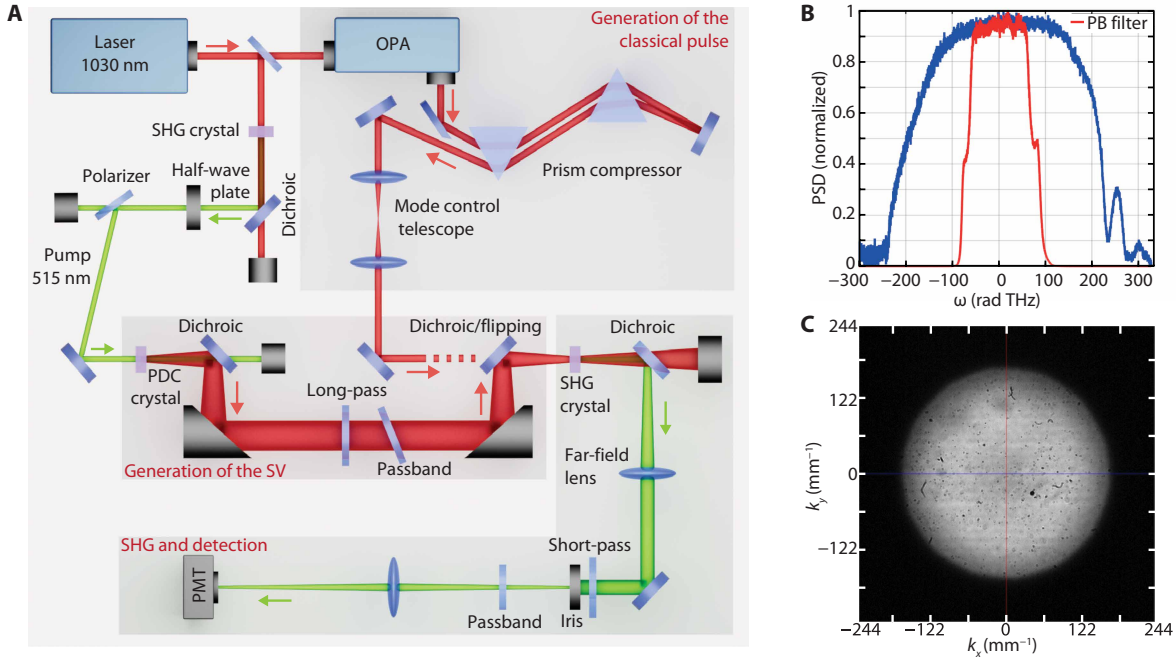

Fig. 1. Experimental configuration. (**A**) Sketch of the experimental setup with the three main building blocks responsible for the SV generation, SHG generation and detection, and the generation of the classical field for comparison. OPA, optical parametric amplifier. (**B**) Power spectral density (PSD) of the SV transmitted by the optical system with (red) and without (blue) the passband (PB) filter. The latter is mainly constrained by the reflectivity of the dichroic mirrors used to reject the 515-nm pump. (**C**) Angular spectrum of the SV after filtering with a 10-nm passband filter centered at 1030 nm.

Characterization of the multimode SV

As the first essential step toward comparing the entangled and classical SHG efficiency, we characterized the SV as a function of the PDC pump energy. This is the most direct control parameter for changing the SV number of photons per mode. To this end, we measured the average number of SV photons generated per pulse, N_{SV}, for increasing number of photons in the PDC pump pulse, N_P. The experimental data (Fig. 2A) show linear photon-pair generation at low PDC gains and nonlinear (quadratic) photon-pair generation at higher gains. We compared these results with the prediction of a quasi-stationary (QS) model for multimode pulsed PDC (*35*, *40*, *41*), using the hypotheses of negligible group velocity mismatch and spatial walk-off between the interacting fields. This model predicts that (see the "Generation of the theory curves" section of the Supplementary Materials)

$$N_{SV} = K_m\left(\Lambda\sqrt{N_P}\right)\sinh^2\left(\Lambda\sqrt{N_P}\right) \quad (1)$$

where $\Lambda = 2\, l_c d_{eff}\sqrt{\frac{\hbar\omega_P\omega_{SV}^2}{2\varepsilon_0 n_P\, n_{SV}^2 c^3\, V_P}}$, l_c is the crystal length, $\omega_{P,SV}$ are the frequencies of the PDC pump and SV, and $n_{P,SV}$ are their refractive indices in the nonlinear crystal, $d_{eff} \simeq 1.79$ pm/V (*42*) is the crystal second-order nonlinear coefficient, and V_P is the pump spatiotemporal volume. We highlight the good matching between the theory (red solid line) and the experimental results (orange data points) in Fig. 2A, under the sole condition of reducing the effective nonlinearity to $d'_{eff} \simeq 1.65$ pm/V, i.e., a <10% difference from the tabulated value. Such a correction is compatible with the effect of the group velocity mismatch, not accounted for by the theoretical curve. In Eq. 1, $\Lambda\sqrt{N_P}$ is the dimensionless parametric gain g, while $\sinh^2\left(\Lambda\sqrt{N_P}\right)$ provides an estimate of the population of the modes (it would be the mean photon number in a simplistic model of single-mode SV at perfect phase-matching) and, from now on, will be referred to as the number of photons per mode $\langle n\rangle_m$. K_m is the number of SV modes, calculated via eq. S4 in the "Generation of the theory curves" section of the Supplementary Materials. It decreases at increasing gain as shown in the inset of Fig. 2B, mainly due to the exponential shrinking of the SV profile (*40*). Note that the model does not account for pump depletion (a valid approximation in the gain regimes considered here), which would quench the shrinking of the number of modes at higher gain. We characterized the SV spatial profile experimentally, as shown in Fig. 2B, for one coordinate, obtaining a good match with the QS model predictions (see also the "Generation of the theory curves" section of the Supplementary Materials).

While a rigorous calculation for K_m requires numerical integration of eq. S4 [see also (*43*)], an estimate can be provided from the ratio of the spatiotemporal size of the SV pulse to the entanglement volume. Under the assumption that the SV pulse profile matches that of the PDC pump (strictly valid only at low parametric gain) and using the previous definition for the entanglement volume, we get $K_m \simeq (185\text{ fs}/45\text{ fs})\times(1500\,\mu\text{m}/22\,\mu\text{m})^2 \simeq 19{,}100$ modes, which is comparable to the value of K_m at low gain shown in Fig. 2B. We note that $\langle n\rangle_m$ is often used to define the bound for the quantum-enhanced regime with the common assumption that the advantage is lost for $\langle n\rangle_m > 1$ and is commonly inferred from N_{SV} assuming a constant number of modes. While K_m is nearly constant in the low-gain PDC $\left(\Lambda\sqrt{N_P} \ll 1\right)$, it decreases steeply for high PDC gain. The value of $\langle n\rangle_m = N_{SV}/K_m\left(N_{SV}\right)$ shown in our plots is, therefore, obtained using the dependence of K_m from the PDC gain given by the theory. In Fig. 2A, we highlight with a green shaded area the region with $\langle n\rangle_m < 1$, where quantum enhancement has been mainly investigated so far. In this work, we show that the enhancement persists for $\langle n\rangle_m > 1$.

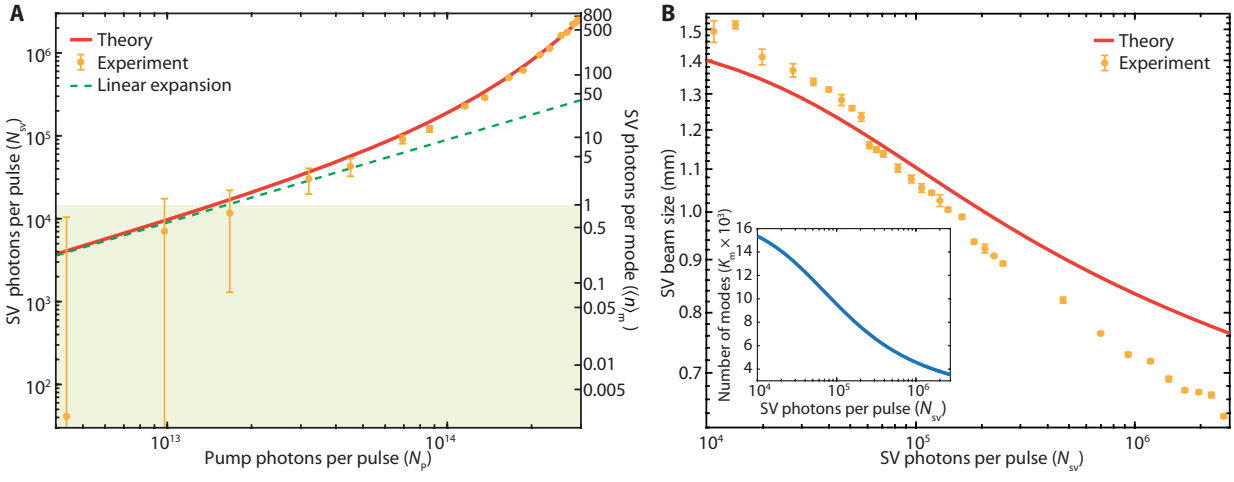

Fig. 2. SV characterization. (**A**) Log-log plot of the number of SV photons per pulse (N_{SV}) versus the number of pump photons per pulse (N_P). The red line is the expected trend predicted by our theoretical model (see text for details), while the green dashed line shows a linear approximation valid in the spontaneous regime. The green shaded area highlights the region where the average number of SV photons per mode $\langle n\rangle_m < 1$ (right axis). The error bars appear asymmetric due to the logarithmic scale. (**B**) Size of the SV beam (intensity FWHM) as a function of the number of SV photons per pulse (N_{SV}), showing a narrowing of the SV volume for increasing gain. The red curve shows the predicted values from the theoretical model. The inset shows the dependence of the number of modes (K_m) from the number of SV photons per pulse (N_{SV}) predicted by the model. We used this curve to evaluate $\langle n\rangle_m = N_{SV}/K_m\left(N_{SV}\right)$.

Loss analysis

Following common practice, we initially investigated the effect of losses on the efficiency of eSHG driven by the SV. Losses degrade the entanglement underpinning quantum enhancement. As a result, a reduction in the eSHG efficiency for a degraded SV state, compared to an unspoiled one with the same mean number of photons per pulse at the SHG crystal, is considered a reliable indicator of quantum enhancement (*11*, *32*). We first focused on the $\langle n \rangle_m < 1$ regime, and we compared the eSHG efficiency of an ideally pure SV with that of a modified state obtained by imposing different losses (30 and 50%) with neutral density filters.

The results for the unspoiled SV (Fig. 3A, green) follow the expected linear trend. Each data point is an average over a 5-min acquisition at 500 kHz, and the error bars show the SD. A generation efficiency $\eta_{SV} = (3.3 \pm 0.2) \times 10^{-10}$ is obtained from the linear fit $N_{SH}^{E} = \frac{\eta_{SV}}{2} N_{SV}$ of our data, where N_{SH}^{E} is the number of eSHG photons per pulse. This compares well with the prediction of the theoretical model $\eta_{SV,th} = 4.3 \times 10^{-10}$ obtained considering only the linear contribution to eSHG (evaluated at $\langle n \rangle_m = 0.05$) and the reduced effective nonlinearity d'_{eff}. We note that the difference (~23%) can be ascribed also to residual losses, aberrations in the imaging system, and dispersion from materials and coatings decreasing the localization of entangled photon pairs in the SHG crystal.

The results obtained by introducing 30 and 50% losses are shown in blue and red, respectively. Note that, to maintain the same photon flux at the SHG crystal, the PDC gain was increased by increasing the pump pulse energy. In these two conditions, the SHG signal can still be fitted considering a linear dependence, albeit with lower generation efficiencies $\eta_{30\%} = (2.2 \pm 0.1) \times 10^{-10}$ and $\eta_{50\%} = (1.3 \pm 0.1) \times 10^{-10}$.

To compare with the results available in the literature, we extracted the trend expected for the eSHG if the SV flux was decreased, for a fixed PDC gain, by introducing increasing losses. Specifically, we selected for the no-loss case the data point corresponding to the maximum number of photons per pulse at the SHG crystal $(\sim 12.6 \times 10^3)$; for the 30% losses, we selected the fit value at $0.7 \times 12.6 \times 10^3$; and for the 50% losses, we selected the fit value at $0.5 \times 12.6 \times 10^3$. These are identified by purple circles in Fig. 3A and, as expected (*11*), match a purely quadratic trend (solid purple curve). This test is crucial to prove the quantum nature of the process (*28*, *44*). It has been shown in eTPA studies that the sole linear scaling for two-photon processes is not necessary evidence of a quantum effect as it could arise from residual single-photon events or by, e.g., hot-band absorption (*26*, *28*, *29*). Notably, from our eSHG results, it is also clear that a linear trend is still visible with spoiled quantum states.

We then increased the PDC pump energy to investigate the unexplored regime of eSHG driven by spatially and temporally multimode SV with $\langle n_m \rangle > 1$. The results for an unspoiled SV, i.e., with no additional losses, are shown in green in Fig. 3B together with those recorded by introducing 60% (blue) and 90% (red) losses. The dashed curves are fits obtained considering a linear plus a quadratic dependence of the SH signal from the input number of photons. Higher values of losses have been chosen here to showcase the competition between quantum correlations and the effects of the increased PDC gain.

We first notice that the efficiency for the no-loss SV is larger than that obtained with a spoiled SV well into the $\langle n \rangle_m > 1$ regime. However, it is also evident that such a trend does not continue indefinitely. The eSHG efficiency for the 90% loss case overcomes that from the no-loss SV at nearly $\langle n \rangle_m \simeq 15$. To understand this effect, it is necessary to recall that higher PDC gain is required to achieve the same photon flux at the SHG crystal for the spoiled SV. As shown before (Fig. 2B), this results in a narrowing of the generated (spoiled) SV field size. Such a reduction results in a higher peak intensity, which thus increases the SHG efficiency despite the reduced quantum correlations. The same effect is predicted by our theoretical

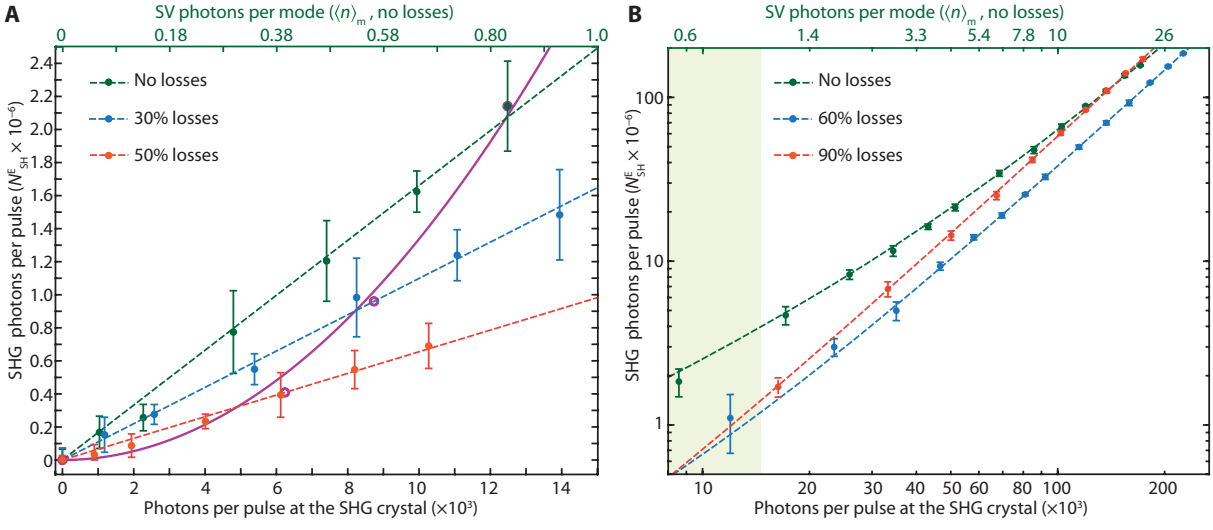

Fig. 3. Loss analysis. (**A**) Measurement of the SHG efficiency: Number of SHG photons per pulse (N_{SH}^{E}) versus number of the input photons on the SH crystal (bottom axis). The top axis reports the number of photons per mode, $\langle n \rangle_m$, for the unspoiled SV case (no losses). The green dots represent the SV input (no losses), while the blue and red dots are for 30 and 50% losses, respectively. The dashed lines are the best fits with a linear function. The purple circles identify the data extracted to have the scaling for fixed SV energy and increasing losses. They follow well a purely quadratic trend (solid purple curve; see text for details). (**B**) Same measurement as in (A) but for higher PDC gain plotted in log-log scale. In this case, we used higher losses (60 and 90%—blue and red, respectively) to enhance the effect. The dashed lines are best fit with a linear plus quadratic term ($y = ax + bx^2$). The green shaded area highlights the region where the unspoiled SV (no losses) has $\langle n \rangle_m \leq 1$.

model (see "Theoretical analysis of the impact of losses" of the Supplementary Materials).

Comparison with a classical field

Following from our investigation on the role of losses, it is clear that to properly assess quantum enhancement, a comparison with a classical field is required. We therefore choose to compare the eSHG efficiency from SV with that of SHG produced by the classical state routinely used for imaging, i.e., a standard laser pulse (a coherent state). The comparison was performed by matching the two intensity profiles, i.e., maintaining the same duration, beam size, and number of photons per pulse. Since the intensity profile of the SV changes with gain, we built a classical source with a tunable beam size and pulse duration, allowing matching to the SV properties, see the "Generation of the classical field" section in Materials and Methods.

The data for the SHG signal generated by the classical source versus the number of pump photons impinging on the crystal (Fig. 4A, red squares) match well the theoretical model (*35*), shown with a red solid curve. In the same figure, we show the results obtained using the SV (green circles) and the theoretical prediction (green solid curve). Both the classical (red) and the entangled (green) theoretical curves have been obtained after multiplying the bare theory results by the same coefficient 0.76, which amounts to the already mentioned correction for the d_{eff} (0.92^2) and to a further 10% efficiency reduction that can be ascribed to losses and residual dispersion effects. It should be noted that in this comparison, the spectrum (spatial and temporal) of the classical pulse is much narrower than the SV one, giving all the advantages to the classical excitation. Yet, it is evident that the SV efficiency is still larger than that of a classical pulse well above the one-photon-per-mode regime, up to an average number of photons per mode $\langle n\rangle_{\mathrm{m}} \simeq 9.3$, confirming our main claim.

It should also be noticed that the experimental data were obtained by carefully optimizing, at each different PDC gain, the position of the SHG crystal with respect to the image plane of the PDC crystal, so to maximize the eSHG rate (the same optimization was done in the theory).

The quantum enhancement obtained using the SV is shown in Fig. 4B, calculated as the ratio between the experimental values of the eSHG and the theoretical values for the classical SHG. In the same graph, we also show the theoretical prediction (green solid curve).

DISCUSSION

The results in Fig. 4A do not include the full SHG signal generated by the SV. Instead, they show the coherent signal induced solely by the up-conversion of entangled photons, namely, the eSHG. As mentioned above, the incoherent (coherent) component is spread over a large (narrow) wave vector spectrum so that the selection is experimentally performed by inserting an iris in the far field of the SH signal and filtering a narrow portion of the SH spectrum, as shown in Fig. 1A. The eSHG signal has a linear component that dominates for low number of SV photons per mode and grows quadratically at increasing SV intensities [also observed in (*26*)], leading to an overall quantum enhancement up to $\langle n_{\mathrm{m}}\rangle \simeq 9.3$. The experimental results match well the outcomes of the theoretical model (*35*) for both the classical and the quantum cases. The model predicts that the maximum $\langle n_{\mathrm{m}}\rangle$ value at which quantum enhancement occurs depends on the experimental parameters and can be further increased from what is reported here. For instance, choosing PDC and SHG crystals of 2- and 1-mm length, respectively, leads to quantum enhancement up to $\langle n_{\mathrm{m}}\rangle \sim 20$ (*35*), albeit resulting in a lower overall SH signal.

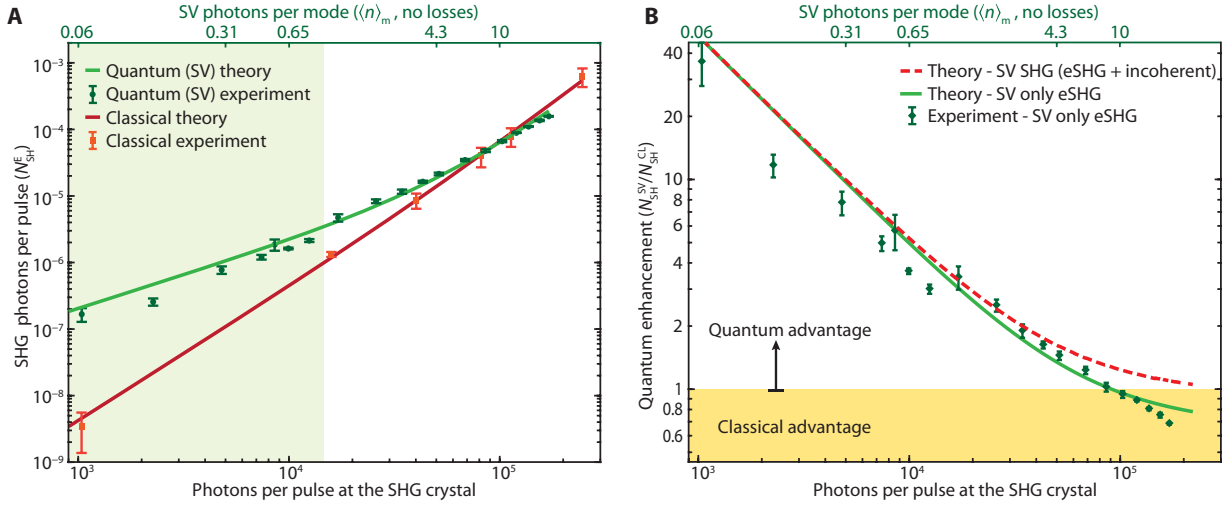

Fig. 4. Comparison with a standard classical field (laser beam). (**A**) SHG signal as a function of the number of photons per pulse at the SHG crystal for the quantum (green) and classical (red) case. A quantum advantage is maintained up to $\langle n\rangle_{\mathrm{m}} \simeq 9.3$ (top axis). The solid curves are the theoretical predictions of the model (*35*) both obtained by considering a reduced $d'_{\mathrm{eff}} \simeq 1.65$ pm/V and 10% overall losses on the SHG signal. The green shaded area highlights the region where the SV has $\langle n\rangle_{\mathrm{m}} \leq 1$. (**B**) Quantum enhancement, defined as the ratio between the SV-driven SHG and the SHG from a classical field (laser), i.e., $N^{SV}_{SH} / N^{CL}_{SH}$. The green diamonds show the ratio between the experimental eSHG values [green circles in (A)] and the theoretical prediction for classical SHG [red curve in (A)]. The green solid curve is the theoretical prediction [ratio between green and red curves in (A)]. The red dashed curve is the theoretical prediction for the total enhancement the SV brings to SHG (coherent and incoherent components; see text for details). The yellow shaded area illustrates the region where the classical case outperforms the SV.

It should be also noted that the theory predicts that the incoherent SH arising from the up-conversion of nonentangled SV photons adds an additional classical quadratic term (*34*). When the contribution from nonentangled photons is also included, the SHG from SV have a larger efficiency than that of a classical field with the same profile independently of the SV intensity (*35*), as shown by the red dashed curve in Fig. 4B.

Our study demonstrates a substantial gain arising from quantum effects in two-photon processes at intensities one order of magnitude larger than what was previously considered feasible. Furthermore, the good agreement between the theory and the experimental results supports the choice of SV as a more efficient field to drive two-photon processes even at intensities for which any quantum advantage was expected to become negligible (*11*, *39*).

MATERIALS AND METHODS

Generation of the quantum field

The pump pulse for the PDC had a 1.5-mm-diameter beam size (FWHM of the intensity profile), a ≃185-fs (FWHM) pulse duration, ≃515-nm central wavelength, and a variable 200/500-kHz repetition rate and was obtained by frequency doubling in a 1-mm-thick BBO crystal (Light Conversion) the ≃245-fs duration, 1030-nm central wavelength output of a Yb:KGW amplified laser (Carbide CB3 40W, Light Conversion). The energy of the PDC pump could be tuned by rotating an achromatic half-wave plate in front of a thin film polarizer (Eksma) in the 1 to 120 μJ per pulse range. The pump was then injected into a 2-mm-long BBO crystal cut for collinear type I SHG of a 1030-nm field coated with antireflection layers (Eksma), where it drove the PDC process resulting into the generation of a broadband multimode SV. This radiation was reimaged into a second BBO crystal identical to the one used for PDC using a confocal imaging system consisting of two 8-inch (20.32-cm) equivalent focal length, 1-inch (2.54-cm) aperture, and 90° off-axis parabolic silver mirrors with broadband ultrafast coatings (low GDD, Edmund Optics) arranged in a 4*f* configuration. The beam path was folded using seven low dispersion dichroic mirrors (Layertec, not all shown in the figure) with high reflectivity (99.9% at an incidence angle of 45°) in a 300-nm bandwidth centered at 1030 nm and with high transmission (>99%) at 515 nm. The low dispersion is required to maintain the temporal localization of the entanglement volume of the SV radiation. To further remove the intense PDC pump (at 515 nm) from the SV, a long-pass filter (FELH0850, Thorlabs) with high optical density at 515 nm was inserted in the beam path. Last, a high transmissivity band-pass filter (Brightline FF01-1055/70-25, Semrock) was also inserted and tuned at ≃23° to cut the SV spectrum symmetrically around the central wavelength of 1030 nm (and to increase the pump rejection further). This way, a sufficient rejection was ensured to avoid contaminating the eSHG signal with residual PDC pump photons. The SV number of photons per pulse N_{SV} was measured with a high-sensitivity calibrated photodiode (S132C, Thorlabs) and background-corrected to remove the contribution from parasitic radiation, e.g., scattering from the laser source.

Entanglement volume

A working definition of the entanglement volume in the SV near-field is $V_{ent} = \pi\rho_{ent}^2\tau_{ent}$ where we made the very simplistic assumption of considering a cylinder of radius ρ_{ent} and length τ_{ent}, where ρ_{ent} and τ_{ent} are the widths (HWHM and FWHM, respectively) of the probability distribution $|\Psi(\vec{\rho},\tau)|^2$ of finding a photon at distance ρ and delay τ from its twin. As described in detail in (*35*, *45*, *46*), the spatiotemporal amplitude probability $\Psi(\vec{\rho},\tau)$ can be written as the Fourier transform of the probability amplitude of finding a photon pair in the conjugate modes $(\vec{q},\Omega)$ and $(-\vec{q},-\Omega)$. This probability amplitude, in turn, can be roughly approximated by the SV spectral intensity profile in the $(\vec{q},\Omega)$ space [see figure 2 in (*35*) for some examples]. From our measurements (see Fig. 1, B and C), we can approximate the SV angular spectrum as a disk of radius $\Delta q \simeq 150\ \mathrm{mm}^{-1}$ and the temporal spectrum as a rectangular function of width $\Delta\Omega \simeq 125$ rad THz. The spatial and temporal profiles of $\Psi(\vec{\rho},\tau)$ are thus described by an Airy disk and a sinc function, respectively. Therefore, the widths of $|\Psi(\vec{\rho},\tau)|^2$ are $\rho_{ent} \simeq 1.62/\Delta q \simeq 10.8\ \mu\mathrm{m}$ (HWHM) and $\tau_{ent} \simeq 5.57/\Delta\Omega \simeq 44.5$ fs (FWHM).

Detection of the eSHG

After the SHG crystal, the residual SV was removed from the beam path with four dichroic mirrors of high reflectivity at 515 nm and

Table 1. Parameters of the classical and SV fields.

Photons at the SHG crystal (10^3/pulse)	Classical beam size (mm, FWHM)	SV beam size (mm, FWHM)	Classical pulse duration (fs, FWHM)
1.0	1.48 ± 0.05		173 ± 5
15.9	1.33 ± 0.05		170 ± 5
19.8		1.41 ± 0.05	
39.9		1.31 ± 0.05	
40.2	1.16 ± 0.05		165 ± 5
81.6	1.07 ± 0.05		158 ± 5
82.6		1.10 ± 0.05	
113.1	1.03 ± 0.05		153 ± 5
117.9		1.04 ± 0.05	
246.9	0.90 ± 0.05		137 ± 5
249.5		0.89 ± 0.05	

high transmission over a large bandwidth (>80 nm) around 1030 nm (Eksma), so that the up-converted signal could be measured with a PMT (H16722P-40, Hamamatsu, 40% quantum efficiency at 515 nm—data rescaled accordingly) connected to a time-to-digital converter (HydraHarp 400, PicoQuant) for the time-gated signal acquisition synchronized to the source pulse train. To select only the coherent signal (eSHG), we filtered the SHG signal by inserting a 1-mm-diameter aperture into the radiation far-field (generated with an $f = 200$-mm focal length lens confocal to the eSHG crystal) and, analogously, by using a narrow-band pass-band filter (10-nm bandwidth around 515 nm). We note that the incoherent SHG radiation in the far-field extended over a ~12-mm-diameter area; therefore, its contribution to the recorded signal (i.e., captured by the 1-mm aperture) was negligible (<0.7%). The SH counts were corrected by subtracting a background measured by rotating the SHG crystal by $\pi/2$ around the surface normal, i.e., in a condition where no conversion occurs.

Generation of the classical field

To generate a coherent classical pulse with the same intensity profile and energy of the SV at different energies, we used the temporally compressed output from an optical parametric amplifier (Orpheus-F, Light Conversion), delivering 1030-nm pulses of ≃120-fs duration. The duration was changed with a prism compressor to match the expected duration of the SV at different energies. Similarly, the beam size was adjusted with telescopes to match the measured SV beam width. In Table 1, we report the values for the energy, pulse duration (measured with a home-built autocorrelator), and beam size of the classical pulse used in the comparison. We also reported the corresponding experimental values for the SV beam size extracted from Fig. 2B at similar energies.

Supplementary Materials

This PDF file includes:

Supplementary Text
Fig. S1

REFERENCES AND NOTES

1. P. T. C. So, C. Y. Dong, B. R. Masters, K. M. Berland, Two-photon excitation fluorescence microscopy. *Annu. Rev. Biomed. Eng.* **2**, 399–429 (2000).
2. F. Helmchen, W. Denk, Deep tissue two-photon microscopy. *Nat. Methods.* **2**, 932–940 (2005).
3. J. D. Bhawalkar, N. D. Kumar, C.-F. Zhao, P. N. Prasad, Two-photon photodynamic therapy. *J. Clin. Laser. Med. Surg.* **15**, 201–204 (1997).
4. B. H. Cumpston, S. P. Ananthavel, S. Barlow, D. L. Dyer, J. E. Ehrlich, L. L. Erskine, A. A. Heikal, S. M. Kuebler, I.-Y. S. Lee, D. McCord-Maughon, J. Qin, H. Röckel, M. Rumi, X.-L. Wu, S. R. Marder, J. W. Perry, Two-photon polymerization initiators for three-dimensional optical data storage and microfabrication. *Nature* **398**, 51–54 (1999).
5. A. Hopt, E. Neher, Highly nonlinear photodamage in two-photon fluorescence microscopy. *Biophys. J.* **80**, 2029–2036 (2001).
6. J. Javanainen, P. L. Gould, Linear intensity dependence of a two-photon transition rate. *Phys. Rev. A* **41**, 5088–5091 (1990).
7. N. P. Georgiades, E. S. Polzik, K. Edamatsu, H. J. Kimble, A. S. Parkins, Nonclassical excitation for atoms in a squeezed vacuum. *Phys. Rev. Lett.* **75**, 3426–3429 (1995).
8. M. C. Teich, B. E. A. Saleh, Entangled-photon microscopy. *Ceskoslovensky casopis pro fyziku* **47**, 3–8 (1997).
9. D.-I. Lee, T. Goodson III, Entangled photon absorption in an organic porphyrin dendrimer. *J. Phys. Chem. B* **110**, 25582–25585 (2006).
10. B. Dayan, A. Pe'er, A. A. Friesem, Y. Silberberg, Two photon absorption and coherent control with broadband down-converted light. *Phys. Rev. Lett.* **93**, 23005 (2004).
11. B. Dayan, A. Pe'er, A. A. Friesem, Y. Silberberg, Nonlinear interactions with an ultrahigh flux of broadband entangled photons. *Phys. Rev. Lett.* **94**, 43602 (2005).
12. D. N. Klyshko, Transverse photon bunching and two-photon processes in the field of parametrically scattered light. *J. Exp. Theo. Phys.* **56**, 753 (1982).
13. B. R. Mollow, Two-photon absorption and field correlation functions. *Phys. Rev.* **175**, 1555–1563 (1968).
14. J. Gea-Banacloche, Two-photon absorption of nonclassical light. *Phys. Rev. Lett.* **62**, 1603–1606 (1989).
15. K. E. Dorfman, F. Schlawin, S. Mukamel, Nonlinear optical signals and spectroscopy with quantum light. *Rev. Mod. Phys.* **88**, 045008 (2016).
16. C. Sánchez Muñoz, G. Frascella, F. Schlawin, Quantum metrology of two-photon absorption. *Phys. Rev. Res.* **3**, 33250 (2021).
17. Y. Chen, R. de J, León-Montiel, L. Chen, Quantum interferometric two-photon excitation spectroscopy. *New J. Phys.* **24**, 113014 (2022).
18. F. Schlawin, Entangled photon spectroscopy. *J. Phys. B* **50**, 203001 (2017).
19. F. Schlawin, K. E. Dorfman, S. Mukamel, Entangled two-photon absorption spectroscopy. *Acc. Chem. Res.* **51**, 2207–2214 (2018).
20. J. P. Villabona-Monsalve, O. Calderón-Losada, M. Nuñez Portela, A. Valencia, Entangled two photon absorption cross section on the 808 nm region for the common dyes zinc tetraphenylporphyrin and rhodamine B. *J. Phys. Chem. A* **121**, 7869–7875 (2017).
21. J. P. Villabona-Monsalve, O. Varnavski, B. A. Palfey, T. Goodson III, Two-photon excitation of flavins and flavoproteins with classical and quantum light. *J. Am. Chem. Soc.* **140**, 14562–14566 (2018).
22. J. P. Villabona-Monsalve, R. K. Burdick, T. Goodson, Measurements of entangled two-photon absorption in organic molecules with CW-pumped type-I spontaneous parametric down-conversion. *J. Phys. Chem. C* **124**, 24526–24532 (2020).
23. T. Li, F. Li, C. Altuzarra, A. Classen, G. S. Agarwal, Squeezed light induced two-photon absorption fluorescence of fluorescein biomarkers. *Appl. Phys. Lett.* **116**, 254001 (2020).
24. S. Corona-Aquino, O. Calderón-Losada, M. Y. Li-Gómez, H. Cruz-Ramirez, V. Álvarez-Venicio, M. D. P. Carreon-Castro, R. de J, León-Montiel, A. B. U'Ren, Experimental study of the validity of entangled two-photon absorption measurements in organic compounds. *J. Phys. Chem. A* **126**, 2185–2195 (2022).
25. M. G. Raymer, T. Landes, M. Allgaier, S. Merkouche, B. J. Smith, A. H. Marcus, How large is the quantum enhancement of two-photon absorption by time-frequency entanglement of photon pairs? *Optica* **8**, 757–758 (2021).
26. T. Landes, B. J. Smith, M. G. Raymer, Limitations in fluorescence-detected entangled two-photon-absorption experiments: Exploring the low- to high-gain squeezing regimes. *Phys. Rev. A* **110**, 033708 (2024).
27. M. G. Raymer, T. Landes, Theory of two-photon absorption with broadband squeezed vacuum. *Phys. Rev. A* **106**, 013717, (2022).
28. A. Mikhaylov, R. N. Wilson, K. M. Parzuchowski, M. D. Mazurek, C. H. Camp, M. J. Stevens, R. Jimenez, Hot-band absorption can mimic entangled two-photon absorption. *J. Phys. Chem. Lett.* **13**, 1489–1493 (2022).
29. B. P. Hickam, M. He, N. Harper, S. Szoke, S. K. Cushing, Single-photon scattering can account for the discrepancies among entangled two-photon measurement techniques. *J. Phys. Chem. Lett.* **13**, 4934–4940 (2022).
30. K. M. Parzuchowski, A. Mikhaylov, M. D. Mazurek, R. N. Wilson, D. J. Lum, T. Gerrits, C. H. J. Camp, M. J. Stevens, R. Jimenez, Setting bounds on entangled two-photon absorption cross sections in common fluorophores. *Phys. Rev. Appl.* **15**, 44012 (2021).
31. T. Landes, M. G. Raymer, M. Allgaier, S. Merkouche, B. J. Smith, A. H. Marcus, Quantifying the enhancement of two-photon absorption due to spectral-temporal entanglement. *Opt. Express* **29**, 20022–20033 (2021).
32. D. Tabakaev, A. Djorović, L. La Volpe, G. Gaulier, S. Ghosh, L. Bonacina, J.-P. Wolf, H. Zbinden, R. T. Thew, Spatial properties of entangled two-photon absorption. *Phys. Rev. Lett.* **129**, 183601 (2022).
33. F. Schlawin, Two-photon absorption cross sections of pulsed entangled beams. *J. Chem. Phys.* **160**, 144117 (2024).
34. K. Y. Spasibko, D. A. Kopylov, V. L. Krutyanskiy, T. V. Murzina, G. Leuchs, M. V. Chekhova, Multiphoton effects enhanced due to ultrafast photon-number fluctuations. *Phys. Rev. Lett.* **119**, 223603 (2017).
35. A. Gatti, M. Clerici, L. Caspani, Enhancing upconversion with space-time entanglement: from twin photons to twin-beams. *Opt. Quantum* **3**, 269–276 (2025).
36. E. Brambilla, O. Jedrkiewicz, L. A. Lugiato, A. Gatti, Disclosing the spatiotemporal structure of parametric down-conversion entanglement through frequency up-conversion. *Phys. Rev. A* **85**, 63834 (2012).
37. O. Jedrkiewicz, J.-L. Blanchet, A. Gatti, E. Brambilla, P. Di Trapani, High visibility pump reconstruction via ultra broadband sum frequency mixing of intense phase-conjugated twin beams. *Opt. Express* **19**, 12903–12912 (2011).
38. O. Jedrkiewicz, A. Gatti, E. Brambilla, P. Di Trapani, Experimental observation of a skewed X-type spatiotemporal correlation of ultrabroadband twin beams. *Phys. Rev. Lett.* **109**, 243901 (2012).
39. B. Dayan, Theory of two-photon interactions with broadband down-converted light and entangled photons. *Phys. Rev. A* **76**, 043813 (2007).
40. A. Gatti, O. Jedrkiewicz, E. Brambilla, Modeling the space-time correlation of pulsed twin beams. *Sci. Rep.* **13**, 16786 (2023).

41. A. Gatti, E. Brambilla, O. Jedrkiewicz, Unified space–time description of pulsed twin beams. *Phil. Trans. R. Soc. A* **382**, 20230334 (2024).
42. R. S. Klein, G. E. Kugel, A. Maillard, A. Sifi, K. Polgár, Absolute non-linear optical coefficients measurements of BBO single crystal and determination of angular acceptance by second harmonic generation. *Opt. Mater.* **22**, 163–169 (2003).
43. A. Gatti, T. Corti, E. Brambilla, D. B. Horoshko, Dimensionality of the spatiotemporal entanglement of parametric down-conversion photon pairs. *Phys. Rev. A* **86**, 053803 (2012).
44. T. Landes, M. Allgaier, S. Merkouche, B. J. Smith, A. H. Marcus, M. G. Raymer, Experimental feasibility of molecular two-photon absorption with isolated time-frequency-entangled photon pairs. *Phys. Rev. Res.* **3**, 033154 (2021).
45. A. Gatti, E. Brambilla, L. Caspani, O. Jedrkiewicz, L. A. Lugiato, X. Entanglement, The nonfactorable spatiotemporal structure of biphoton correlation. *Phys. Rev. Lett.* **102**, 223601 (2009).
46. L. Caspani, E. Brambilla, A. Gatti, Tailoring the spatiotemporal structure of biphoton entanglement in type-I parametric down-conversion. *Phys. Rev. A* **81**, 033808 (2010).

Acknowledgments
Funding: This work was supported by Innovate UK, BQS, project reference 10075401 (D.F. and M.C.); UKRI, Fellowship "In-Tempo," EP/S001573/1 (M.C.); Royal Academy of Engineering, Chair in Emerging Technologies (D.F.); EPSRC, EP/Y029097/1 (D.F.); EPSRC, EP/V051148/1 (C.M.); European Commission (ERC) Consolidator Grant, QuNIm, G.A. 101125923 (M.C. and L.C.); UKRI and EPSRC, EP/V062492/1 (L.C.); UKRI and EPSRC, "QuantIC," EP/T00097X/1 (I.A., C.M., M.C., and L.C.); Studentship funding support from Fraunhofer UK Research Ltd (T.D.); and PRIN 2022K3KMX7 of the MUR ELISE, CUP B53D2300515000 (T.D., O.J., A.G., and M.C.). **Author contributions:** Conceptualization: D.F., C.M., A.G., M.C., and L.C. Methodology: T.D., I.A., O.J., D.F., C.M., A.G., M.C., and L.C. Formal analysis: T.D., I.A., G.A., L.H., A.G., M.C., and L.C. Investigation: T.D., I.A., G.A., S.N., M.C., and L.C. Theoretical model: A.G. Writing—original draft: T.D., I.A., A.G., M.C., and L.C. Writing—review and editing: All authors. Visualization: T.D., I.A., A.G., M.C., and L.C. Supervision: D.F., C.M., M.C., and L.C. Project administration: M.C. and L.C. **Competing interests:** The authors declare that they have no competing interests. **Data and materials availability:** Data are available at the following repository: DOI: 10.15129/b13c036e-4ae2-4ae3-8dcc-7b9c4de103f5.

Submitted 4 February 2025
Accepted 29 May 2025
Published 4 July 2025
10.1126/sciadv.adw4820